


A Systematic Approach to Improve Scatter Sensitivity of a Flow Cytometer for Detection of Extracellular Vesicles

Leonie de Rond,^{1,2,3*}  Edwin van der Pol,^{1,2,3} Paul R. Bloemen,¹ Tina Van Den Broeck,⁴ Ludo Monheim,⁴ Rienk Nieuwland,^{2,3} Ton G. van Leeuwen,^{1,3} Frank A.W. Coumans^{1,2,3}

¹Biomedical Engineering and Physics, Amsterdam UMC, University of Amsterdam, Amsterdam, The Netherlands

²Laboratory Experimental Clinical Chemistry, Amsterdam UMC, University of Amsterdam, Amsterdam, The Netherlands

³Vesicle Observation Center, Amsterdam UMC, University of Amsterdam, Amsterdam, The Netherlands

⁴BD Biosciences, Erembodegem, Belgium

Received 9 July 2019; Revised 6 November 2019; Accepted 6 January 2020

Grant sponsor: Netherlands Organisation for Scientific Research, Grant number: VENI 13681, Grant number: VENI 15924, Grant number: STW Perspectief Program CANCER-ID 14195

Additional Supporting Information may be found in the online version of this article.

*Correspondence to: Leonie de Rond, Department of Biomedical Engineering and Physics, Cancer Center Amsterdam, Amsterdam Cardiovascular Sciences, Amsterdam UMC, University of Amsterdam, Meibergdreef 9, 1105AZ Amsterdam, The Netherlands
 Email: l.derond@amsterdamumc.nl

Published online in Wiley Online Library (wileyonlinelibrary.com)

DOI: 10.1002/cyto.a.23974

• Abstract

Extracellular vesicles (EVs) are commonly studied by flow cytometry. Due to their small size and low refractive index, the scatter intensity of most EVs is below the detection limit of common flow cytometers. Here, we aim to improve forward scatter (FSC) and side scatter (SSC) sensitivity of a common flow cytometer to detect single 100 nm EVs. The effects of the optical and fluidics configuration on scatter sensitivity of a FACSCanto (Becton Dickinson) were evaluated by the separation index (SI) and robust coefficient of variation (rCV) of polystyrene beads (BioCytex). Improvement is defined as increased SI and/or reduced rCV. Changing the obscuration bar improved the rCV 1.9-fold for FSC. A 10-fold increase in laser power improved the SI 19-fold for FSC and 4.4-fold for SSC, whereas the rCV worsened 0.8-fold and improved 1.5-fold, respectively. Confocalization worsened the SI 1.2-fold for FSC, and improved the SI 5.1-fold for SSC, while the rCV improved 1.1-fold and worsened 1.5-fold, respectively. Replacing the FSC photodiode with a photomultiplier tube improved the SI 66-fold and rCV 4.2-fold. A 2-fold reduction in sample stream width improved both SI and rCV for FSC by 1.8-fold, and for SSC by 1.3- and 2.2-fold, respectively. Decreasing the sample flow velocity worsened rCVs. Decreasing the flow channel dimensions and the pore size of the sheath filter did not substantially change the SI or rCV. Using the optimal optical configuration and fluidics settings, the SI improved 3.8·10⁴-fold on FSC and 30-fold on SSC, resulting in estimated detection limits for EVs (assuming a refractive index of 1.40) of 246 and 91 nm on FSC and SSC, respectively. Although a 50-fold improvement on FSC is still necessary, these adaptations have produced an operator-friendly, high-throughput flow cytometer with a high sensitivity on both SSC and FSC. © 2020 The Authors. *Cytometry Part A* published by Wiley Periodicals, Inc. on behalf of International Society for Advancement of Cytometry.

• Key terms

exosomes; extracellular vesicles; flow cytometry; light scattering; microparticle

Cells release membrane-enclosed particles into their environment to communicate or to transport waste. These membrane-enclosed particles are called extracellular vesicles (EVs) and are present in all body fluids. EVs are potential biomarkers, because their concentration and composition in body fluids change with disease (1–4).

Flow cytometry is often applied to characterize EVs in body fluids, because of its high throughput and ability to distinguish between different EV populations at single-EV level based on immunophenotype (5). Figure 1A shows that the majority of EVs in human urine have a diameter <200 nm (6). In plasma, at least 47% of EVs have a diameter <200 nm (8). A recent study involving multiple centers that use flow cytometry to study EVs (7) showed that most flow cytometers do not detect EVs <200 nm based on scatter (Fig. 1A). In fact, only 6 out of the 46 flow cytometers could detect a scatter of 300 nm EVs or smaller. Moreover, due to the power-law relation between

© 2020 The Authors. *Cytometry Part A* published by Wiley Periodicals, Inc. on behalf of International Society for Advancement of Cytometry.

This is an open access article under the terms of the Creative Commons Attribution-NonCommercial-NoDerivs License, which

permits use and distribution in any medium, provided the original work is properly cited, the use is non-commercial and no modifications or adaptations are made.

EV concentration and diameter, the detected size range of a flow cytometer strongly affects the measured EV concentration, as shown in Figure 1B. For example, a 3-fold increase of the detected size range from >300 to >100 nm results in a 15-fold increase in the measured EV concentration.

Multiple efforts have been described toward increasing the sensitivity of a flow cytometer for the detection of sub-micrometer particles (9–18). Most efforts focused on improving the side scatter (SSC) sensitivity (9–13). SSC is the logical choice when a single sensitive scatter detector is required, because SSC has a dark field configuration. From the signals of a single scatter detector, it is generally possible to derive particle size if the particle refractive index is known (19–21). However, if the refractive index is unknown, only the ratio of SSC versus forward scatter (FSC) allows simultaneous determination of particle size and refractive index (22). The refractive index proved useful to distinguish EVs from non-EV particles, such as lipoproteins, which are abundantly present in plasma (23). Regardless of whether fluorescence- or scatter-based detection is used, sensitive SSC and FSC detections are required to allow determination of particle size and refractive index. In addition, none of the previous reports (9–18) showed a systematic and quantitative overview of the influence of an adaptation on the sensitivity of the flow cytometer. Such a systematic overview would provide insight in the relative contributions of the different adaptations to improve sensitivity and can indicate future directions for improvements.

Here, we systematically evaluated adaptations to the optical configuration and fluidics of a common flow cytometer (FACSCanto, Becton Dickinson [BD], Franklin Lakes, NJ), and show the resulting effects on the FSC, SSC, and fluorescence sensitivity. The evaluated adaptations include varying the obscuration bar shape, laser power, pin-hole diameter, detector type, sample stream width, sample flow velocity, flow channel dimensions, and the pore size of the sheath filter. The aim is to enable detection of scatter signals from 100 nm EVs on both the FSC and SSC detectors.

MATERIALS AND METHODS

Materials

A mixture of green fluorescent polystyrene (PS) beads of 100, 300, 500, and 900 nm (Megamix-plus FSC, Stago BNL, Leiden, the Netherlands) was used to evaluate flow cytometer sensitivity with every adaptation. The sensitivity of the optimized system was demonstrated using nonfluorescent 100 ± 7.8 , 125 ± 4.5 , 147 ± 4.3 , 203 ± 5.3 , 400 ± 7.3 nm NIST traceable PS beads (mean \pm standard deviation [SD], all 3000 Series Nanosphere Size Standards, Thermo Fischer Scientific, Rockford, IL), 75 ± 7.7 nm silica bead (mean \pm SD, Supporting Information Fig. S1, SI-0.1, Kisker Biotech GmbH, Steinfurt, Germany), 189 ± 2 and 374 ± 10 nm hollow silica beads (mean \pm uncertainty, (24)) and a urine EV sample.

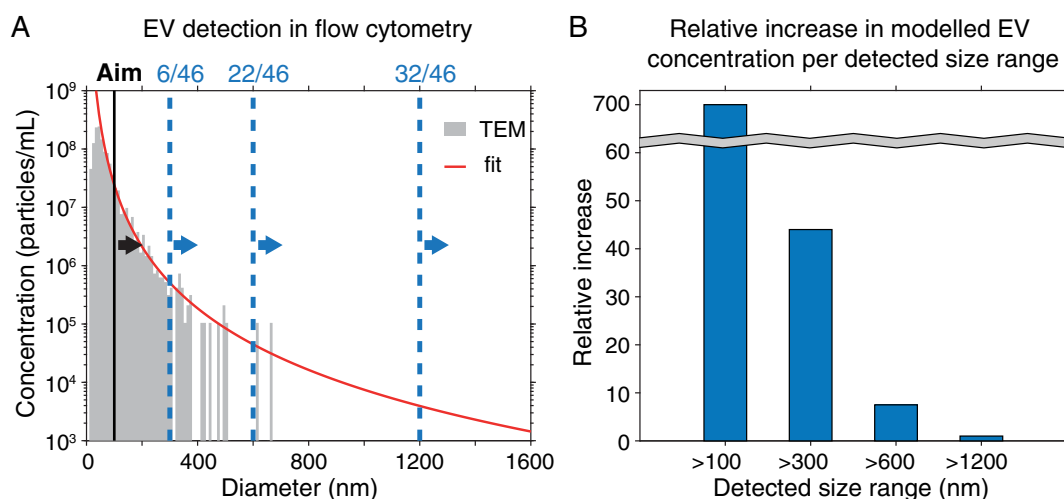


Figure 1. Extracellular vesicle (EV) detection by common flow cytometers. **(A)** Size distribution of urinary EVs ($n = 5$) as measured by transmission electron microscopy (TEM) and fitted with a power law (red line) (6). Of the 46 flow cytometers tested in (7), 32 could detect EVs >1,200 nm, 22 EVs >600 nm, and only 6 could detect EVs >300 nm. Here, we aim to enable detection of EVs >100 nm (black line). **(B)** Increase in detected EV concentration as a function of the detected size range relative to the concentration of EVs >1,200 nm. [Color figure can be viewed at wileyonlinelibrary.com]

Urine EV Sample

Urine from five overnight fasting healthy male donors was collected and processed as described earlier (25). Informed consent and approval from the ethics committee was obtained. Briefly, urine was pooled and centrifuged for 10 min at 180 g, 4°C, followed by 20 min at 1,560 g, 4°C to remove cells. Aliquots of 1 ml of the resulting cell-free urine were snap-frozen in liquid nitrogen and stored at -80°C. Before use, 12 aliquots of cell-free urine were thawed at 37°C, pooled, and centrifuged for 10 min at 1,560 g, 4°C to remove salt precipitation. The resulting cell- and salt-precipitate-free supernatant was diluted in phosphate-buffered saline (PBS, 21-031-CVR, Corning, Corning, NY) before analysis.

Flow Cytometer Adaptations

We systematically evaluated adaptations to the optical configuration and fluidics ($N = 1$ for all configurations) of a FACSCanto flow cytometer (Fig. 2A). Upon hardware adaptations, FACSCanto should only be used for research purposes and cannot be used for diagnostic purposes.

Optical configuration

Obscuration bars with different designs were obtained from BD (cat# 641570 and 647895). Among the tested obscuration bar designs are the standard design (#1 in Fig. 3A), a symmetrical and asymmetrical vertical design (#2 and #3 in Fig. 3A), a cross design (#4 in Fig. 3A), and a round design (#5 in Fig. 3A). The vertical designs were tested because the laser is shaped as a vertical ellipse at the position of the obscuration bar, in which Obscuration bar 3 was intended to represent a slightly broader version of Obscuration bar 2. The cross design was tested as a thicker version of the standard design and the round design was tested because it blocks a uniform angle of light. For each FSC detection module, all obscuration bars

were tested and the optimal one for that module was identified and used during all subsequent analysis with the module. The standard 20 mW laser of the FACSCanto was replaced with a 20–200 mW adjustable power laser (both 488 nm Sapphire, Coherent, Santa Clara, CA).

The standard SSC detection module of the FACSCanto (Supporting Information Fig. S2A) contains a pinhole with a diameter of 1,000 μm . Here we tested an SSC module (BD, Supporting Information Fig. S2B) with a 105, 200, or 400 μm fiber (Thorlabs, Newton, NJ), which acts as a spatial pinhole, to see if further confocalization (i.e., decreasing the pinhole size) improves scatter sensitivity. Increased confocalization decreases the contribution of background scattered light (e.g., scattering of the channel walls and particles in the sheath; Fig. 2A) and thereby decreases the noise, thus potentially improving the sensitivity. Under the assumption that particles pass through the focus of the collection lens, and because the image of the particle is at least 14-fold smaller than the pinhole, the pinhole does not affect the collection angles.

The standard FSC detection module (Supporting Information Fig. S2A) contains a photodiode (PD) and an obscuration bar to prevent the illuminating laser light from reaching the detector. Here, we confocalized FSC detection by replacing the standard FSC detection module with the dual FSC module (BD, Supporting Information Fig. S2B). In addition to an obscuration bar, the dual FSC module also contains a numerical aperture (NA) ~ 0.2 lens and 400 μm pinhole. Next to a PD, the dual FSC module contains a photomultiplier tube (PMT), which typically has lower detector noise than PDs.

Subsequently, a prototype tube FSC detection module (BD, Supporting Information Fig. S2C) was tested, which consists of a PMT, a 6.7 \times magnifying lens set and a 100 μm pinhole to enable better separation between sample stream and

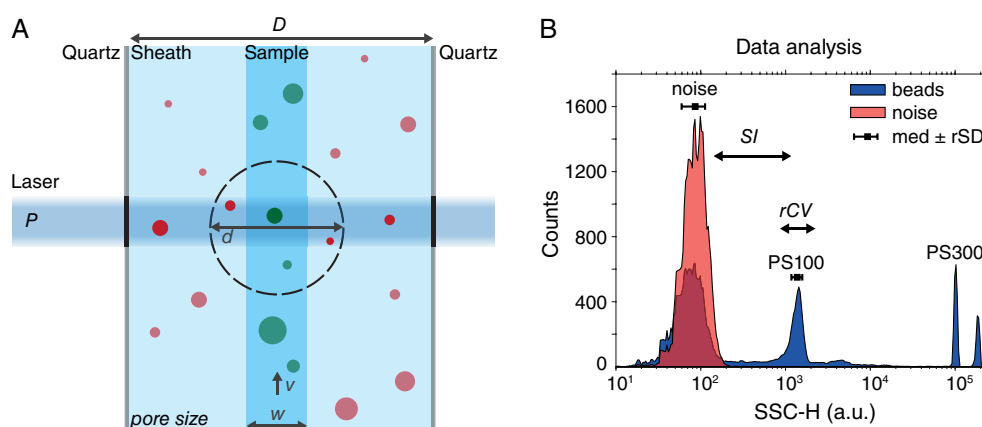


Figure 2. (A) Schematic representation of the adaptations made to increase sensitivity. Depicted is the channel inside the cuvette (black lines), containing the sheath stream with particles (red circles) and sample stream with particles (green circles). A projection of the detector pinhole (dashed black line) is also shown. Here we investigated how the scatter sensitivity depends on laser power (P), pinhole diameter (d), sample stream width (w), sample flow velocity (v), flow channel dimensions (D), and the pore size of the sheath filter. (B) Side scatter (SSC-H) histogram of beads (blue) and noise (red). The median intensity (med, black squares) and robust standard deviation (rSD, whiskers) are used to calculate the separation index (SI) and robust coefficient of variation (rCV) according to Eqs. 1 and 2. The SI thereby is a measure for the separation between a bead population and the noise, and the rCV for the reproducibility of the system. PS100, 100 nm polystyrene (PS) bead population; PS300, 300 nm PS bead population. [Color figure can be viewed at wileyonlinelibrary.com]

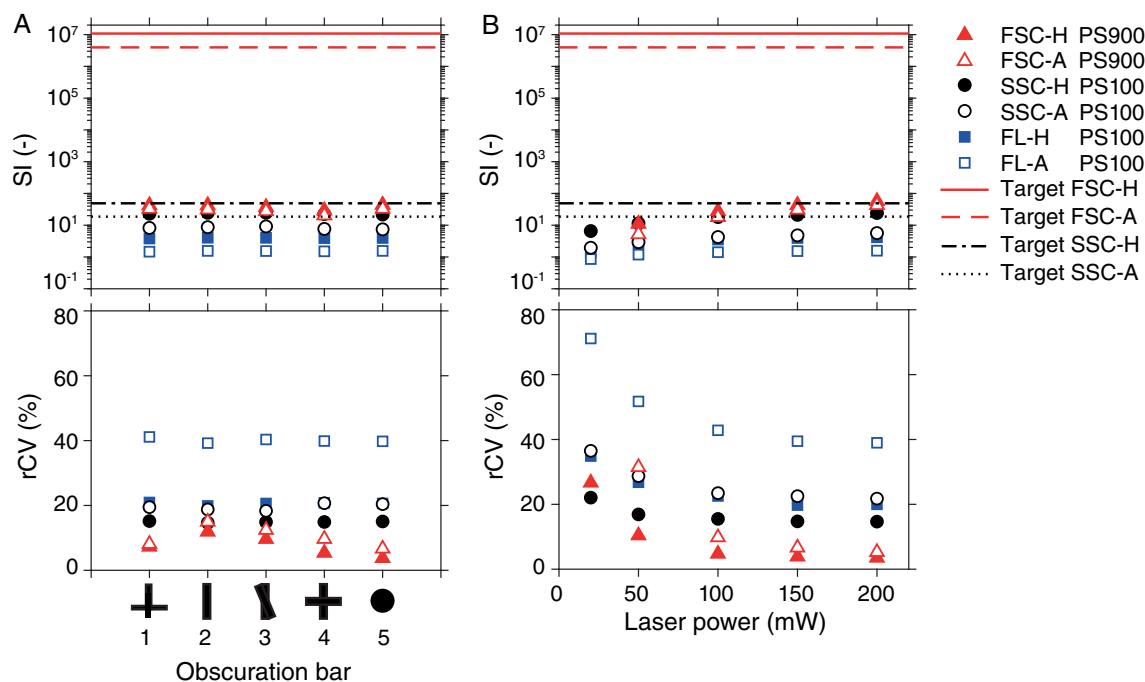


Figure 3. Influence of (A) forward scatter (FSC) obscuration bar shape and (B) laser power on the separation index (SI, top panels) and robust coefficient of variation (rCV, bottom panels). For FSC (red triangles), data of 900 nm polystyrene (PS) are shown, for side scatter (SSC, black circles) and fluorescence (FL, blue squares) data of 100 nm PS are shown. The required SI for the depicted PS bead to allow detection of 100 nm extracellular vesicles for FSC (red lines) and SSC (black lines) as calculated using Mie theory are also shown. Data collected using standard flow cytometer set up. A, area parameter; H, height parameter. [Color figure can be viewed at wileyonlinelibrary.com]

background signals. This design was optimized using simulations in Zemax (Zemax LLC, Kirkland, WA), and the resulting optimized tube FSC detection module (Supporting Information Fig. S2D) containing a 6.5 \times magnifying lens set and a 100, 200, or 300 μ m pinhole (all Thorlabs) was tested.

Fluidics

The sample stream width (w in Fig. 2A) was varied by adjusting the sample pressure in the Diva software (BD). The resulting sample width was determined by running a fluorescent sample (diluted ink from yellow Stabilo Boss marker, Staples, Framingham, MA) and imaging the flow channel with a home-built 2.8 \times microscope. The sample width was defined as the full width at half the maximum of the fluorescence intensity in the captured image.

The sample flow rate (v in Fig. 2A) was reduced by reducing the sheath flow rate, which due to the design of the flow cell determines the sample flow velocity. The sheath flow rate reduced by placing an adjustable flow tubing clip (Fisher Scientific, Hampton, NH) on the sheath tubing. The sheath flow rate was measured by mass discharge and we confirmed a reciprocal relationship between the width parameter and the measured sheath flow rate (Supporting information, Fig. S5). While reducing the sheath flow rate, the sample stream width was monitored by microscopy (see previous paragraph) and kept constant by reducing the sample flow rate using a syringe pump (11Plus, Harvard apparatus, Holliston, MA). Another way to reduce the sample flow velocity is by decreasing the dimensions of the flow

channel (D in Fig. 2A) in the cuvette. A narrower flow channel has a higher flow resistance, thereby causing a reduction in sample flow velocity. Here, we tested a cuvette (Hellma, Jena, Germany) with an inner flow channel of half the dimensions of the standard one. The sampling rate of the analog-to-digital converter was 10 MHz for all adaptations. Lastly, the standard 0.2 μ m sheath filter was replaced with a 0.1 μ m filter (Millipak-100, Merck Chemicals, Darmstadt, Germany).

Flow Cytometry Analysis

To optimize the hardware (Figs. 2–5), green fluorescence of the Megamix-plus FSC beads was detected in the fluorescein isothiocyanate (FITC) channel (530/30 band-pass filter) and in the phycoerythrin (PE) channel (585/42 band-pass filter). The fluorescence detected in the FITC channel was used to trigger data acquisition, to ensure detection of all beads throughout the adaptations. The fluorescence detected in the PE channel was used to monitor the effect of the adaptations on the fluorescence sensitivity, and as a control. The Megamix beads were diluted in 10-fold concentrated PBS (BE17-525F, Lonza, Basel, Switzerland) and purified and deionized water to obtain Megamix beads in 1-fold concentrated PBS. A minimum of 1,000 events per bead population were acquired. Noise levels were estimated by measuring PBS while triggering on the FITC channel with low threshold (200 arbitrary units [a.u.]) and high voltage (600 V). The resulting randomly triggered events enable an approximation of FSC and SSC noise.

To enable determination of the separation index (SI), and thereby monitor the sensitivity, both noise and bead signal need to be within the dynamic range of the detector. Thereto, the PMT voltage was adjusted after every adaptation, according to a standardized protocol. The voltage on the FITC channel was configured to attain a rate of 1000 (noise) events/s in PBS using FITC triggering. Next, the SSC voltage was set such that the 300 nm bead had an intensity of 10^5 a.u., and the PE voltage such that the 500 nm bead had an intensity of 10^4 a.u. Since only the 900 nm bead was detectable on FSC in the standard configuration, the FSC PMT voltage was instead configured to center the noise in the FSC channel around 10^2 a.u. At the used PMT voltages, the optical noise is dominant over the electronic noise for all channels (robust SD [rSD] with laser off $\leq 2.5 \cdot \text{rSD}$ with laser on), except for SSC after the illumination and detection adaptations. After these adaptations, the noise on SSC was no longer within the dynamic range using the 300 nm bead setting approach, so for the fluidics experiments the noise on SSC was also centered around 10^2 a.u. with the PMT voltage, causing the optical noise to be dominant again. For a complete description of the flow cytometer configuration, operating conditions and data analysis, see the MIFlowCyt list in Supporting Information Data S1.

To demonstrate the sensitivity of the optimized system (Fig. 6), we triggered on SSC to enable detection of non-fluorescent beads. Noise levels were estimated by triggering on the FITC channel, as described before.

Data Analysis

The SI and rCV (Fig. 2B) for each bead population were calculated as follows:

$$SI = \frac{\text{median}_{\text{bead}} - \text{median}_{\text{noise}}}{2 \cdot \text{rSD}_{\text{noise}}}, \quad (1)$$

$$\text{rCV} = \frac{\text{rSD}_{\text{bead}}}{\text{median}_{\text{bead}}} \cdot 100\%, \quad (2)$$

with $\text{median}_{\text{bead}}$ the median intensity of the bead population, $\text{median}_{\text{noise}}$ the median intensity of the noise, and $\text{rSD}_{\text{noise}}$ and rSD_{bead} the robust SD of the noise and bead, respectively, defined as

$$\text{rSD} = \mathcal{S}(\text{percentile}_{84.13} - \text{percentile}_{15.87}), \quad (3)$$

with $\text{percentile}_{84.13}$ and $\text{percentile}_{15.87}$ the intensity of the noise or bead population at those percentiles. Eq. 1 was selected in analogy to the Stain Index (26), which is commonly used to express brightness in fluorescence. The rCV was preferred over the CV because the rCV is less affected by outliers. Data analysis was done in Matlab R2018b (Mathworks, Natick, MA). The SI and rCV were calculated for both the height and area parameters. Data for both parameters are given in the figures. However, the SI on the area parameter was negative for some configurations, making expressions of fold changes between configurations meaningless. Therefore, under the condition that the area and height

parameters show the same trend, the text contains only quantitative statements of the height parameter. For SSC and fluorescence, data of the 100 nm bead are shown in all figures. For FSC, the bead used to follow progress differs per figure, as a result of large improvements in sensitivity. Throughout this manuscript, an improvement in sensitivity is defined as an increase in SI >1 -fold and/or a reduction in rCV >1 -fold.

Mie Theory

Scatter versus diameter relations were calculated for the standard and optimized FACSCanto FSC and SSC detection modules as described previously (19), using Mie theory and a bead mixture with beads of known size and refractive index (Exometry, Amsterdam, the Netherlands). Since the standard FSC detection module detects only one bead of the bead mixture, modeling of the optical configuration of the FSC detection module was performed by manual calculations based on geometry. Using the scatter versus diameter relations, the scatter intensities in a.u. can be linked to the corresponding scattering cross section (σ_s) in nm^2 .

The scatter intensity of a 100 nm EV can be derived from the scatter versus diameter relation for EVs (assuming a refractive index of 1.40 throughout this manuscript unless stated otherwise). Assuming that the noise shape is conserved (i.e., SD/median will stay the same), the required noise median to achieve an SI of 1 for a 100 nm EV can be derived from Eq. 1. With the scatter versus diameter relation for PS, this noise median can be translated into an SI needed for any specific size PS bead, at which 100 nm EVs will then be detectable. The resulting SIs are depicted as the “target” in Figures 3–5. See Supplemental Information Appendix S1 for a detailed description of the calculation of the target values. Furthermore, using the measured noise distributions on the standard and optimized FACSCanto, the median signal at which an SI of 2 is achieved can be calculated from Eq. 1. The detection limits for EVs were subsequently derived from the scatter versus diameter relations for EVs with a refractive index ranging between 1.37 (22,27) and 1.40 (28,29).

RESULTS

Optical Configuration

Figure 3A shows the effect of the obscuration bar shape on the SI and rCV in the standard flow cytometer. Since the obscuration bar is in the detection path of FSC only, no differences were expected nor observed for SSC and fluorescence. Figure 3A shows that the obscuration bar shape mainly affected the rCV for FSC, with minor variations in the SI (<1.5 -fold). The latter can be explained by the fact that the noise suppression reaches a maximum once the entire laser beam is blocked, which is the case for all tested obscuration bars. A possible explanation for the changes in rCV is that variations in the FSC intensity due to the position of the particle in the sample stream are more efficiently canceled out by one obscuration bar than the other. The round obscuration bar (#5 in Fig. 3A) resulted in the lowest rCV (1.9-fold improvement) in the standard flow cytometer, and also for

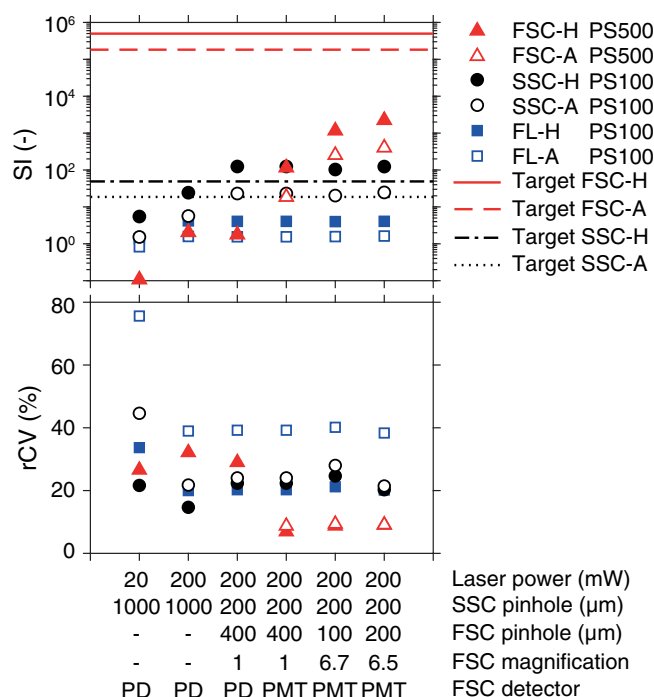


Figure 4. Influence of laser power in combination with adaptations in the detection modules on the separation index (SI, top panels) and robust coefficient of variation (rCV, bottom panels). For forward scatter (FSC, red triangles), data of 500 nm PS are shown, for side scatter (SSC, black circles) and fluorescence (FL, blue squares) data of 100 nm PS are shown. Lines represent the required SI for the depicted PS bead to allow detection of 100 nm extracellular vesicles for FSC (red lines) and SSC (black lines), as calculated using Mie theory. A, area parameter; H, height parameter; PD, photodiode, PMT, photomultiplier tube. [Color figure can be viewed at wileyonlinelibrary.com]

the other FSC modules (data not shown). Therefore, we used the round obscuration bar in all further experiments.

Figure 3B shows the effect of the laser power on the SI and rCV in the standard flow cytometer. An increased laser power resulted in an improved SI and rCV for all detectors. Because the scattered power is linearly proportional to the illuminating power, an increase in laser power increases the number of scattered photons, thereby increasing the SI and decreasing rCV according to photon statistics.

Figure 4 shows the influence of laser power in combination with adaptations in the FSC and SSC detection modules on the SI and rCV. The first column of the graphs shows the SI and rCV for the standard FACSCanto. Increasing the laser power from 20 to 200 mW (second column), improved the SI 19-fold for FSC, 4.4-fold for SSC, and 3.0-fold for fluorescence. The 10-fold increase in laser power could achieve a 19-fold improvement in SI for FSC because $\text{SI} < 1$ at 20 mW. The rCV thereby worsened 1.2-fold for FSC and improved 1.5-fold for SSC and 1.7-fold for fluorescence. Confocalization (third column) worsened the SI 1.2-fold for FSC and improved the SI 5.1-fold for SSC. The rCV improved 1.1-fold for FSC and worsened 1.5-fold for SSC. Replacing the 200 μm fiber on SSC for a 105 μm fiber did not improve SSC

sensitivity (e.g., worsened the SI 2.5-fold and the rCV 2.7-fold, data not shown). The 400 μm fiber improved the rCV 1.6-fold, but worsened the SI 1.2-fold (data not shown). As shown by the SI of the 100 nm PS bead relative to the target, the combination of increased laser power and the 200 μm fiber enabled detection of 100 nm EVs on SSC (third column). Since we thereby reached our aim for SSC detection, further modifications to the optical configuration were focused on the FSC module. Replacement of the FSC PD with a PMT in the confocalized setup (fourth column), improved the SI on FSC 66-fold and the rCV 4.2-fold. Addition of two magnifying lens sets and reduction of the pinhole diameter (fifth column) improved the SI 10-fold, with only a slight worsening of the rCV (1.3-fold). Optimization of this setup by replacing the two magnifying lens sets with a single one led to another 1.9-fold improvement in the SI while keeping the rCV similar (improvement of 1.0-fold, sixth column). Changing the 200 μm pinhole for a 100 or 300 μm pinhole did not improve FSC sensitivity (SI worsened >1.4 -fold, data not shown).

All together, the SI improved $2.1 \cdot 10^4$ -fold for FSC, 23-fold for SSC, and 2.9-fold for fluorescence due to adaptations in the optical configuration, and the rCV improved 2.9-fold for FSC, 1.1-fold for SSC, and 1.7-fold for fluorescence. We continued with the optimized optical configuration (last column) to study the influence of adaptations in the fluidics on the SI and rCV.

Fluidics

Figure 5A shows the influence of the sample stream width on the SI and rCV. The sample flow rate was kept constant during these experiments. Reducing the sample stream width from 25 to 12 μm improved the SI 1.8-fold for FSC, 1.3-fold for SSC, and 1.0-fold for fluorescence. The rCV thereby improved 1.8-fold for FSC, 2.2-fold for SSC, and 1.1-fold for fluorescence.

The influence of the sheath flow rate, and thereby sample flow velocity, on the SI and rCV is shown in Figure 5B. The sample stream width was kept constant during these experiments. Here, the height parameter and the area parameter show a different trend. While the SI of the height parameter does not change (1.1-fold improvement for FSC, 1.5-fold worsening for SSC, 1.1-fold improvement for fluorescence), the SI of the area parameter does. This can be explained by the fact that a longer transit time will result in light being scattered by the particle over a longer period of time, so the integrated scattered light over time will be higher (i.e. area parameter), but the maximal amplitude of the scattered light per time point will not change significantly (i.e. height parameter). For the area parameter, a 17.5-fold reduction in sample flow velocity improved the SI 15-fold for FSC, 7.7-fold for SSC, and 9.6-fold for fluorescence. The area rCV, however, worsened 2.8-fold for FSC, 2.5-fold for SSC, and improved 2.5-fold for fluorescence. Also, the height rCV increased with decreasing flow rate. Such increases in the rCV are undesirable, since high rCVs indicate poor reproducibility and decrease resolution.

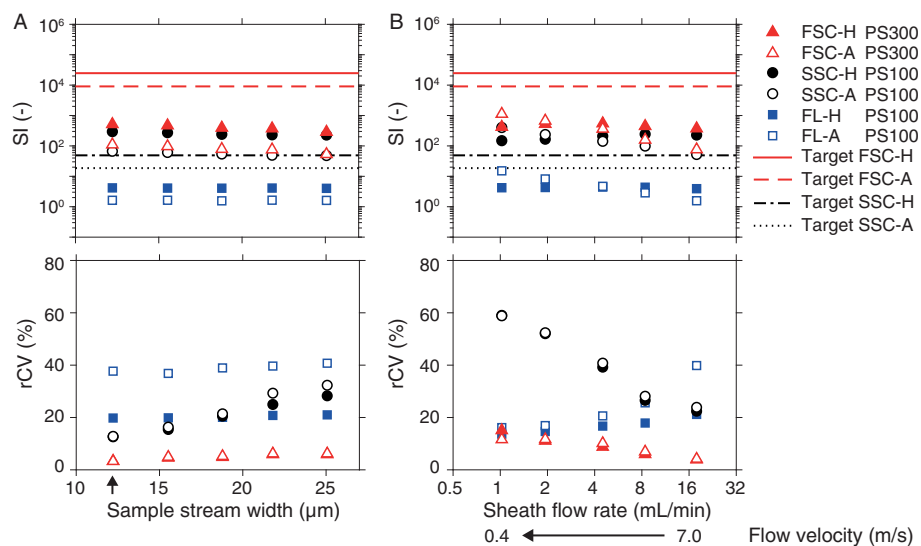


Figure 5. Influence of (A) sample stream width and (B) sample flow velocity on the separation index (SI, top panels) and robust coefficient of variation (rCV, bottom panels). For forward scatter (FSC, triangles), data of 300 nm PS are shown, for side scatter (SSC, black circles) and fluorescence (FL, blue squares) data of 100 nm PS are shown. Lines represent the required SI for the depicted PS bead to allow detection of 100 nm extracellular vesicles for FSC (red lines) and SSC (black lines), as calculated using Mie theory. Data collected using optimal detection setup (Fig. 4, right column). Sensitivity of the final optimized FACSCanto as indicated by the arrow in panel A. A, area parameter; H, height parameter. [Color figure can be viewed at wileyonlinelibrary.com]

Combining a low sample flow velocity (0.4 m/s, 1 mL/min) with a low sample stream width (12 μm) slightly improved the rCVs, but still resulted in an rCV of 45% for SSC (Supporting Information Fig. S3). The overall gain in FSC SI is thereby small (1.9-fold compared to decreasing the sample stream width alone). Taken together, the tested reductions in sample flow velocity do not improve the scatter sensitivity of this system. Similarly, a 2-fold reduction in the dimensions of the flow channel in the cuvette did not result in substantial changes in the SI or rCV (Supporting Information Fig. S3). The latter could be explained by the fact that the contribution of background light is higher in a narrower flow channel, because the walls of the flow channel are closer to the sample stream and thus to the detector pinhole. In addition, reducing the pore size of the sheath filter from 0.2 to 0.1 μm did not change the SI or rCV (Supporting Information Fig. S3). Changing the filters thus did not reduce the noise level.

With regard to the fluidics, only decreasing the sample stream width improved the scatter sensitivity of the flow cytometer in this study. The optimized FACSCanto thus has the sensitivity as depicted in Figure 5A at a sample stream width of 12 μm (arrow in Fig. 5A).

EV Measurement

To demonstrate the sensitivity of the optimized FACSCanto, beads and EVs isolated from human urine were measured using SSC thresholding on both the optimized FACSCanto (Fig. 6A,C) and a standard FACSCanto II (Fig. 6B,D), which has a comparable sensitivity to the standard FACSCanto. PMT voltages on both instruments were set according to the

protocol described in “Materials and Methods” section, and a low sample flow rate was used on the FACSCanto II.

Figure 6A shows that on the optimized FACSCanto, the 189 and 374 nm hollow silica beads can easily be detected on SSC. On FSC, the 374 nm hollow silica bead is almost separated from the noise. On the standard FACSCanto (Fig. 6B), both hollow silica beads cannot be detected. On the optimized FACSCanto, 100 nm PS is 2 decades from the noise on SSC, whereas on the standard FACSCanto it is still indiscernible from the noise. The smallest detectable bead (SI > 1) on the optimized FACSCanto is 75 nm silica on SSC and 150 nm PS on FSC. On the standard FACSCanto, the smallest detectable bead is 125 nm PS on SSC and >400 nm PS on FSC.

Since the 75 nm silica beads were close to the detection limit, there is a risk of swarm detection, meaning that hundreds of particles are simultaneously illuminated and wrongly detected as single particles (21). To exclude swarm detection of 75 nm silica beads, we determined the size distribution of the beads by transmission electron microscopy (Supporting Information Fig. S1) to (1) confirm absence of contaminations <75 nm, which may contribute to swarm detection, and (2) determine the mean size and total concentration of the beads. Next, we diluted the silica beads to a concentration of $10^7/\text{ml}$, at which only 1–2.5% of the events is caused by the simultaneous presence of two silica beads (Supporting Information Fig. S4). The fact that the measured bead concentration was only a factor 2 lower than expected, thereby excludes swarm and coincidence detection. Figure S6 of the Supporting Information shows a calibration of the SSC-H detector using Mie theory to further confirm that single 75 nm silica beads indeed exceed the trigger threshold.

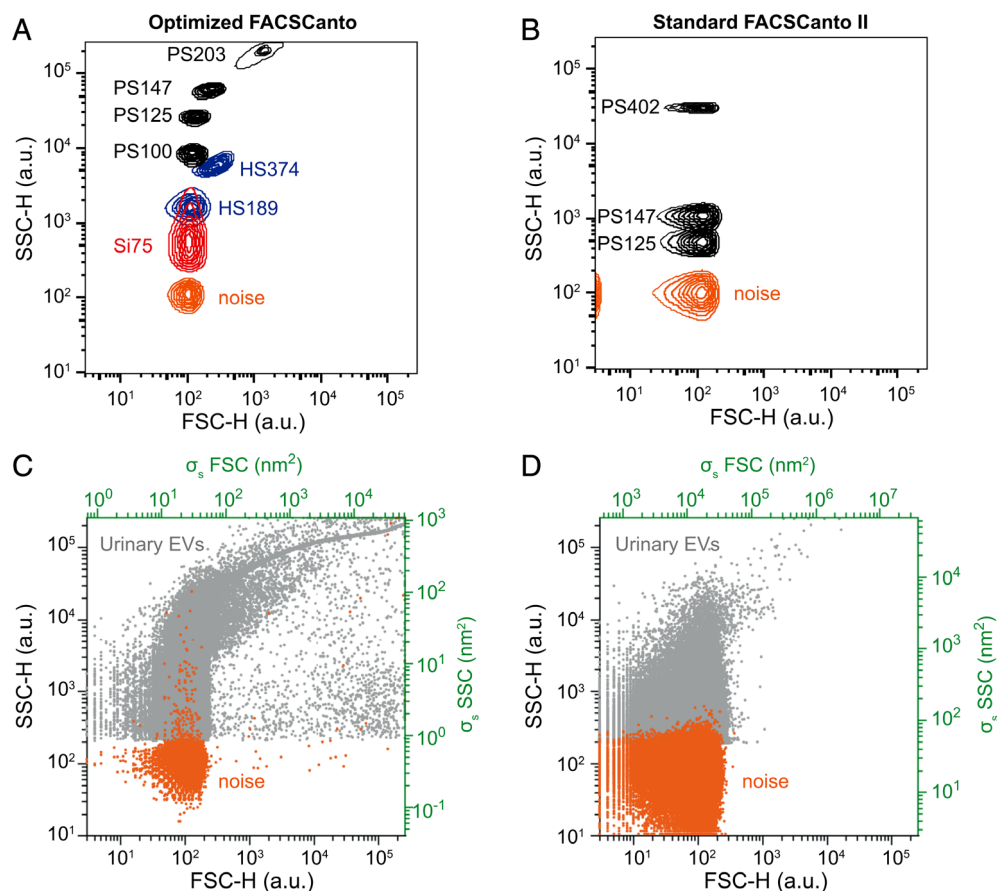


Figure 6. (A,B) Contour plots of side (SSC-H) versus forward scatter (FSC-H) for beads and noise on the optimized FACSCanto (A) and standard FACSCanto II (B). Noise data acquired using a trigger on the fluorescein isothiocyanate (FITC) channel as described in “Materials and Methods” section. (C,D) scatter plots of SSC-H versus FSC-H for urinary extracellular vesicles (gray dots) and noise (orange) as measured on the optimized FACSCanto (C) and standard FACSCanto II (D). Bottom and left axes (black) show the scattering intensities in arbitrary units (a.u.), top and right axes (green) show the corresponding scattering cross section (σ_s) in nm^2 as described in “Materials and Methods” section. Data of the height (H) parameter are shown, since these data showed a better separation from the noise. Si, silica; HS, hollow silica; PS, polystyrene; Si75, 75 nm silica beads. [Color figure can be viewed at wileyonlinelibrary.com]

Figure 6C,D shows clear differences between the FSC versus SSC plots of the urine EVs on both flow cytometers. In addition to the standard axis in a.u., the calibrated axis in terms of the measured σ_s in nm^2 is shown. The σ_s of a 100 nm EV (refractive index 1.40) and 75 nm silica beads (refractive index 1.463) for SSC on the optimized FACSCanto are 1.52 and 1.31 nm^2 , respectively. Since these values for σ_s exceed the σ_s of the noise in Figure 6C, modeling thus shows that 100 nm EVs and 75 nm silica beads are separated from the noise on SSC of the optimized FACSCanto. Furthermore, the calibrated axis show that the optimized FACSCanto allows detection of signals that are two orders of magnitude lower on SSC, and three orders of magnitude lower on FSC compared to the standard FACSCanto.

DISCUSSION

In this study, we systematically evaluated adaptations to the optical configuration and fluidics of a common flow

cytometer, the FACSCanto, and showed the resulting effects on the FSC, SSC, and fluorescence sensitivity.

rCVs were found to worsen slightly upon increased confocalization for SSC, which is because the 200- μm pinhole diameter is near the projected width of the imaged sample stream at the pinhole ($\sim 150 \mu\text{m}$). This configuration leads to sample position-dependent transmission of light through the pinhole, with the highest transmission for particles that travel through the center of the pinhole. A magnifying lens set added to FSC allowed optimization of the projected width of the sample stream at the pinhole and the pinhole diameter, using commercially available pinholes. A decreased sample stream width enabled further optimization resulting in improved rCVs and slight improvements in the SI. Previous work suggested that the pinhole diameter should be twice the projected sample stream diameter to achieve low rCVs (17). Here, the final system has a 12 μm wide sample stream, which results in a 96 μm projected sample stream diameter for SSC, and 78 μm for FSC, which compared to the 200 μm pinholes used indeed results in a factor of ~ 2 .

Several studies increased the sensitivity of their flow cytometer by increasing the transit time of the particle in the laser beam, that is, decreasing the sample flow velocity (10,12). Unexpectedly, for this system, the rCV on FSC and SSC worsened when decreasing the sample flow velocity, even though we adjusted the sample flow rate to the sheath flow rate to maintain the same sample stream width. Analysis of the sample stream width revealed a 1.86-fold increase in the sample stream width with decreasing flow velocity, which was found to be partly due to diffusion of the fluorescent dye molecules into the sheath. For EV particle sizes, however, diffusion is at least 50-fold smaller, and therefore unlikely to play a role. Another explanation for the observed worsening in rCV could be that the fluidics becomes less stable due to the restriction on the sheath flow rate, or the design of the cuvette and cuvette holder. Fluidic instability can cause fluctuations in the position of the sample stream, which will worsen rCVs as not all scattered light will be collected with equal efficiency by the pinholes.

With the exception of the worsened rCVs at low sample flow velocities, the effects of the adaptations described in this study are expected to be similar for at least all BD flow cytometers incorporating a cuvette, and possibly all flow cytometers. The described adaptations can therefore be used to increase the sensitivity of any (BD) flow cytometer. Except for the adaptation of the sample flow velocity, the effects of the adaptations were thereby similar for the height and area parameter. For FSC, the highest impact was changing the PD for a PMT (66-fold SI improvement). For SSC, both increased laser power and reduced pinhole diameter caused a similar improvement in the SI (4.4- and 5.1-fold, respectively).

The adaptations in the optical configuration and fluidics resulted in a total improvement of the SI on FSC of $3.8 \cdot 10^4$ -fold, on SSC of 30-fold, and on fluorescence of 2.9-fold. As a result, the estimated detection limits (SI = 2) for EVs (refractive index between 1.37–1.40 (22,27–29)) changed from 1,228–1,571 nm on FSC and 182–272 nm on SSC for the standard FACSCanto, to 246–310 nm on FSC and 91–117 nm on SSC for the optimized FACS Canto. On FSC, another ~50-fold improvement is needed to allow detection of 100 nm EVs. A possible way to further increase the FSC sensitivity is by using a 405 nm laser instead of 488 nm, which has been shown to increase the scattered light intensity for SSC ~2-fold (30) and should be effective for FSC as well. Another way would be to increase the laser power >200 mW, and/or to increase the NA. The latter will require modification of the SSC objective holder, since this is now physically obstructing the realization of a large NA on FSC. Another route toward improved sensitivity might be to improve the signal processing. In addition to hardware adaptations, this will require adaptation of the software, which is why we did not explore this route in the current study.

As shown in Figure 6A, the smallest detectable bead (SI > 1) on the optimized FACSCanto is 75 nm silica on SSC and 150 nm PS on FSC. The SSC sensitivity is thereby better than or comparable to reported in previously mentioned work (better than References 9,13–18,31, comparable to Reference 11).

Only the NanoFCM (10,12) has a higher SSC sensitivity of 24 nm silica beads. For FSC, only the Beckman Coulter MoFlo Asterios (31) has a comparable and the BD Influx (16) a better sensitivity than our optimized FACSCanto. Both the NanoFCM and BD Influx, however, are not suited to be used in routine (clinical) labs, the NanoFCM because of its low count rate (~200 events/s (10)), and the BD Influx because it requires the permanent presence of a highly skilled operator. Here, we thus present the first operator-friendly, high-throughput flow cytometer with a high sensitivity on SSC and FSC, enabling the determination of EV size and refractive index in human body fluids.

ACKNOWLEDGMENTS

This work was supported by the Netherlands Organisation for Scientific Research—Domain Applied and Engineering Sciences (NWO-TTW), research programmes VENI 13681 (F.A.W.C.), VENI 15924 (E.v.d.P.), and STW Perspectief program CANCER-ID 14195 (L.d.R.). Tina Van Den Broeck and Ludovic Monheim are both employees of BD Biosciences, a business unit of Becton, Dickinson and Company. Frank A.W. Coumans and Edwin van der Pol are co-founder and stakeholder of Exometry B.V., Amsterdam, the Netherlands.

REFERENCES

- O'Driscoll L. Expanding on exosomes and ectosomes in cancer. *N Engl J Med* 2015; 372:2359–2362.
- Loyer X, Vion A-C, Tedgui A, Boulanger CM. Microvesicles as cell–cell messengers in cardiovascular diseases. *Circ Res* 2014;114:345–353.
- Yuana Y, Sturk A, Nieuwland R. Extracellular vesicles in physiological and pathological conditions. *Blood Rev* 2013;27:31–39.
- Robbins PD, Morelli AE. Regulation of immune responses by extracellular vesicles. *Nat Rev Immunol* 2014;14:195–208.
- Coumans FAW, Brisson AR, Buzas EI, Dignat-George F, Drees EEE, El-Andaloussi S, Emanuelli C, Gasecka A, Hendrix A, Hill AF, et al. Methodological guidelines to study extracellular vesicles. *Circ Res* 2017;120:1632–1648.
- van der Pol E, Coumans FAW, Grootemaat AE, Gardiner C, Sargent IL, Harrison P, Sturk A, van Leeuwen TG, Nieuwland R. Particle size distribution of exosomes and microvesicles determined by transmission electron microscopy, flow cytometry, nanoparticle tracking analysis, and resistive pulse sensing. *J Thromb Haemost* 2014; 12:1182–1192.
- van der Pol E, Sturk A, van Leeuwen T, Nieuwland R, Coumans F. Standardization of extracellular vesicle measurements by flow cytometry through vesicle diameter approximation. *J Thromb Haemost* 2018;16:1236–1245.
- Arraud N, Linares R, Tan S, Gounou C, Pasquet JM, Mornet S, Brisson AR. Extracellular vesicles from blood plasma: Determination of their morphology, size, phenotype and concentration. *J Thromb Haemost* 2014;12:614–627.
- Stoner SA, Duggan E, Condello D, Guerrero A, Turk JR, Narayanan PK, Nolan JP. High sensitivity flow cytometry of membrane vesicles. *Cytometry A* 2016;89: 196–206.
- Zhu S, Ma L, Wang S, Chen C, Zhang W, Yang L, Hang W, Nolan JP, Wu L, Yan X. Light-scattering detection below the level of single fluorescent molecules for high-resolution characterization of functional nanoparticles. *ACS Nano* 2014;8: 10998–11006.
- Steen HB. Flow cytometer for measurement of the light scattering of viral and other submicroscopic particles. *Cytometry A* 2004;57A:94–99.
- Yang L, Zhu S, Hang W, Wu L, Yan X. Development of an ultrasensitive dual-channel flow cytometer for the individual analysis of nanosized particles and biomolecules. *Anal Chem* 2009;81:2555–2563.
- Hercher M, Mueller W, Shapiro HM. Detection and discrimination of individual viruses by flow cytometry. *J Histochem Cytochem* 1979;27:350–352.
- Danielson KM, Estanislau J, Tigges J, Toxavidis V, Camacho V, Felton EJ, Khoory J, Kreimer S, Ivanov AR, Mantel P-Y, et al. Diurnal variations of circulating extracellular vesicles measured by nano flow cytometry. *PLoS One* 2016;11:e0144678.
- Steen HB. Simultaneous separate detection of low angle and large angle light scattering in an arc lamp-based flow cytometer. *Cytometry* 1986;7:445–449.
- Nolte-t Hoen ENM, van der Vlist EJ, Aalberts M, Mertens HCH, Bosch BJ, Bartelink W, Mastrobattista E, van Gaal EVB, Stoorvogel W, Arkesteijn GJA, et al. Quantitative and qualitative flow cytometric analysis of nanosized cell-derived membrane vesicles. *Nanomedicine* 2012;8:712–720.
- Zarrin F, Risfelt JA, Dovichi NJ. Light scatter detection within the sheath flow cuvette for size determination of multicomponent submicrometer particle suspensions. *Anal Chem* 1987;59:850–854.

18. Chandler WL, Yeung W, Tait JF. A new microparticle size calibration standard for use in measuring smaller microparticles using a new flow cytometer. *J Thromb Haemost* 2011;9:1216–1224.
19. de Rond L, Coumans FAW, Nieuwland R, van Leeuwen TG, van der Pol E. Deriving extracellular vesicle size from scatter intensities measured by flow cytometry. *Curr Protoc Cytom* 2018;86:e43.
20. Welsh JA, Horak P, Wilkinson JS, Ford VJ, Jones JC, Smith D, Holloway JA, Englyst NA. FCM PASS software aids extracellular vesicle light scatter standardization. *Cytometry A* 2019.
21. van der Pol E, van Gemert MJC, Sturk A, Nieuwland R, Van Leeuwen TG. Single vs. swarm detection of microparticles and exosomes by flow cytometry. *J Thromb Haemost* 2012;10:919–930.
22. van der Pol E, de Rond L, Coumans FAW, Gool EL, Böing AN, Sturk A, Nieuwland R, van Leeuwen TG. Absolute sizing and label-free identification of extracellular vesicles by flow cytometry. *Nanomedicine* 2018;14:801–810.
23. de Rond L, Libregts SFWM, Rikkert LG, Hau CM, van der Pol E, Nieuwland R, van Leeuwen TG, Coumans FAW. Refractive index to evaluate staining specificity of extracellular vesicles by flow cytometry. *J Extracell Vesicles* 2019;8:1643671.
24. Varga Z, van der Pol E, Pálmai M, Garcia-Diez R, Gollwitzer C, Krumrey M, Fraikin J-L, Gasecka A, Hajji N, van Leeuwen TG, et al. Hollow organosilica beads as reference particles for optical detection of extracellular vesicles. *J Thromb Haemost* 2018;16:1646–1655.
25. Rikkert LG, Nieuwland R, Terstappen LWMM, Coumans FAW. Quality of extracellular vesicle images by transmission electron microscopy is operator and protocol dependent. *J Extracell Vesicles* 2019;8:1555419.
26. Maecker HT, Frey T, Nomura LE, Trotter J. Selecting fluorochrome conjugates for maximum sensitivity. *Cytometry A* 2004;62A:169–173.
27. van der Pol E, Coumans FAW, Sturk A, Nieuwland R, van Leeuwen TG. Refractive index determination of nanoparticles in suspension using nanoparticle tracking analysis. *Nano Lett* 2014;14:6195–6201.
28. Gardiner C, Shaw M, Hole P, Smith J, Tannetta D, Redman CW, Sargent IL. Measurement of refractive index by nanoparticle tracking analysis reveals heterogeneity in extracellular vesicles. *J Extracell Vesicles* 2014;3:25361.
29. Konokhova AI, Yurkin MA, Moskalensky AE, Chernyshev AV, Tsvetovskaya GA, Chikova ED, Maltsev VP. Light-scattering flow cytometry for identification and characterization of blood microparticles. *J Biomed Opt* 2012;17:0570061–0570068.
30. McVey MJ, Spring CM, Kuebler WM. Improved resolution in extracellular vesicle populations using 405 instead of 488 nm side scatter. *J Extracell Vesicles* 2018;7:1454776.
31. Morales-Kastresana A, Musich TA, Welsh JA, Telford W, Demberg T, JCS W, Bigos M, Ross CD, Kachynski A, Dean A, et al. High-fidelity detection and sorting of nanoscale vesicles in viral disease and cancer. *J Extracell Vesicles* 2019;8:1597603.